

Highly improved supercapacitance properties of MnFe₂O₄ nanoparticles by MoS₂ nanosheets

Samira Sharifi

Tarbiat Modares University

Kourosh Rahimi

Tarbiat Modares University

Ahmad Yazdani (✉ yazdania@modares.ac.ir)

Tarbiat Modares University

Research Article

Keywords: Molybdenum disulfide, Manganese ferrite, Hydrothermal synthesis, Supercapacitor, Density functional theory

Posted Date: December 28th, 2020

DOI: <https://doi.org/10.21203/rs.3.rs-132314/v1>

License: © ⓘ This work is licensed under a Creative Commons Attribution 4.0 International License.

[Read Full License](#)

Version of Record: A version of this preprint was published at Scientific Reports on April 16th, 2021. See the published version at <https://doi.org/10.1038/s41598-021-87823-6>.

Highly improved supercapacitance properties of MnFe₂O₄ nanoparticles by MoS₂ nanosheets

Samira Sharifi, Kourosh Rahimi, and Ahmad Yazdani*

Condensed Matter Physics Group, Department of Basic Sciences, Tarbiat Modares University, Jalal-Ale-Ahmad Avenue, Tehran, Iran.

*Corresponding author: yazdania@modares.ac.ir

Abstract

Manganese ferrite (MnFe₂O₄) nanoparticles were synthesized via a hydrothermal method and combined with exfoliated MoS₂ nanosheets, and the nanocomposite was studied as a supercapacitor. X-ray diffractometry and Raman spectroscopy confirmed the crystalline structures and structural characteristics of the nanocomposite. Field-emission scanning electron microscopy images showed the uniform and dense distribution of MnFe₂O₄ nanoparticles (~10 nm) on few-layer MoS₂ nanosheets (~2 to 3 μm in width). UV-visible absorption photospectrometry indicated a decrease in the bandgap of MnFe₂O₄ by MoS₂, resulting in a higher conductivity that is suitable for capacitance. Electrochemical tests showed that the incorporation of MoS₂ nanosheets largely increased the specific capacitance of MnFe₂O₄ from 600 to 2093 F/g (with the corresponding energy density and power density of 46.51 Wh/kg and 213.64 W/kg, respectively) at 1 A/g, and led to better charge-discharge cycling stability. We also demonstrated a real-world application of the MnFe₂O₄/MoS₂ nanocomposite in a two-cell asymmetric supercapacitor setup. A density functional theory study was also performed on the MnFe₂O₄/MoS₂ interface to analyze how a MoS₂ monolayer can enhance the electronic properties of MnFe₂O₄ towards a higher specific capacitance.

Keywords: Molybdenum disulfide; Manganese ferrite; Hydrothermal synthesis; Supercapacitor; Density functional theory

1. Introduction

There have been increasing demands in the past few decades for superior energy storage and conversion devices to address the basic energy-related needs of the ever-growing population in the world ¹. Therefore, it is indispensable to develop energy-storage devices with high energy capacities, long lifetimes, and high cycling stability to overcome the impending exhaustion of fossil fuel reserves and alleviate environmental concerns ². Supercapacitors are among the most-promising energy-storage devices owing to their longer lifespan than secondary batteries and their higher capacitance and reliability than conventional dielectric capacitors ². There are two classifications for supercapacitors based on their energy storage mechanisms: (1) electrochemical double-layer capacitors that accumulate charges at their electrode/electrolyte interface and (2) pseudocapacitors that handle charges via fast and reversible redox reactions on electrochemically active sites ³. However, it is yet challenging to design and develop electrode materials to realize these anticipated features and efficiently store/deliver energy ⁴⁻⁶.

There has been recently growing attention to two-dimensional (2D) layered materials for a variety of applications including energy production and storage, sensors, photocatalysts, etc ^{7,8}. Recent developments suggest that 2D transition metal dichalcogenides (TMDs) such as MoS₂, MoSe₂, WS₂, TiS₂, NbS₂, and VS₂ have great potential to fill the gap between the current performance and the modern requirements of energy-storage devices as electrodes of electrochemical supercapacitors ⁹⁻¹². In general, TMDs make use of fast and reversible faradaic redox reactions (also known as pseudocapacitance) that involve ions and electrons in their charge storage mechanism ^{13,14}. In particular, few-layer MoS₂

nanosheets have been found promising because of their large surface area, which acts as a substrate to hold other nanoparticles, and high thermal stability¹⁵.

Among various transition metals¹⁶, nickel, manganese, and cobalt are most promising in the field of supercapacitance due to their high electrochemical activity and low cost as well as the abundance of their oxide/hydroxide compounds^{17–21}. It has also been demonstrated that the spinel ferrites of these metals (MFe_2O_4 , M is a transition metal) deliver much better electrochemical performance due to their richer valence electron, different redox states, synergistic effects between their metal ions, electrochemical stability, and chemical and mechanical stability, suitable for batteries and supercapacitors^{13,22}. Recently, we have compared the supercapacitance of MnFe_2O_4 , CoFe_2O_4 , and NiFe_2O_4 nanoparticles, and found that MnFe_2O_4 exhibits better supercapacitance properties^{13,14}.

It is thus interesting to make composites of MnFe_2O_4 nanoparticles and few-layer MoS_2 nanosheets, as a 2D TMD, to utilize their synergistic effects to achieve improved electronic properties^{23,24}. In such a composite, the MnFe_2O_4 nanoparticles would prevent the MoS_2 nanosheets from restacking, and in a similar manner, the MoS_2 nanosheets would act as a substrate on which the MnFe_2O_4 nanoparticles can be uniformly distributed so that they would not be agglomerated. The mutual effect would result ultimately in a larger active surface area that can promote electrolyte access and provide more channels for ions' and electrons' transfer²⁵.

To the best of our knowledge, there is not yet any report on supercapacitance properties of the composite of MoS_2 nanosheets (as a TMD) decorated with MnFe_2O_4 (as a metal ferrite) nanoparticles, and it is thus interesting to see how the probable synergistic effect of them can be useful to achieve improved electrochemical energy storage performance. Here, we reported the successful fabrication of a $\text{MnFe}_2\text{O}_4/\text{MoS}_2$ nanocomposite on nickel foam via a facile hydrothermal method and tested the nanocomposite as a supercapacitor electrode.

2. Experimental

Manganese(II) nitrate tetrahydrate ($\text{Mn}(\text{NO}_3)_2 \cdot 4\text{H}_2\text{O}$), iron(III) nitrate nonahydrate ($\text{Fe}(\text{NO}_3)_3 \cdot 9\text{H}_2\text{O}$), cetyltrimethylammonium bromide (CTAB), N-Methyl-2-pyrrolidone (NMP), acetonitrile, polyvinylidene difluoride (PVDF), activated carbon (AC), and hydrogen peroxide (H_2O_2) were purchased from Merck Co. (>98%) and bulk molybdenum disulfide (MoS_2 , 99%) powder was purchased from Sigma-Aldrich Co, and the precursors were used without any further purification.

2.1. Synthesis

Few-layer MoS_2 nanosheets were exfoliated from bulk MoS_2 powder in mixed solvents based on the work of Lu et al.²⁶. First, 20 mg MoS_2 powder was mixed in 0.5 ml acetonitrile and it was ground for 1 h. The obtained powder was mixed in a solution of 30 wt% H_2O_2 and NMP (H_2O_2 :NMP volume ratio = 1:19), and it was stirred for 10 h at 35 °C to be exfoliated. The mixture was dried in a furnace for 5 h at 300 °C to evaporate NMP. To in-situ synthesize the $\text{MnFe}_2\text{O}_4/\text{MoS}_2$ nanocomposite on a Ni foam substrate using a hydrothermal method, 0.1 g of the obtained MoS_2 nanosheets was first dispersed into 40 ml deionized water, and 0.4 g $\text{Fe}(\text{NO}_3)_3 \cdot 9\text{H}_2\text{O}$, 0.125 g $\text{Mn}(\text{NO}_3)_2 \cdot 4\text{H}_2\text{O}$, and 0.125 g CTAB were dissolved into the dispersion by stirring for 2 h. Next, 1 ml of 25% ammonia solution was added into the prepared mixture under vigorous stirring until its pH reached ~9. The obtained mixture was transferred into a Teflon-lined autoclave and a nickel foam substrate, cut in the size of $1 \times 2 \text{ cm}^2$, and cleaned with deionized water, acetone, and ethanol, was put into it. The autoclave subsequently heated in an oven at 180 °C for 15 h, and then it was allowed to cool to room temperature in ambient air. Finally, the $\text{MnFe}_2\text{O}_4/\text{MoS}_2$ -coated nickel foam was washed several times with deionized water and ethanol and dried in an oven at 80 °C for 2 h. For comparative purposes, MnFe_2O_4 -coated nickel foam was also synthesized via a similar method without adding MoS_2 . The prepared substrates were used for further characterizations. Fig. 1 shows a schematic of various steps followed in our synthesis procedure.

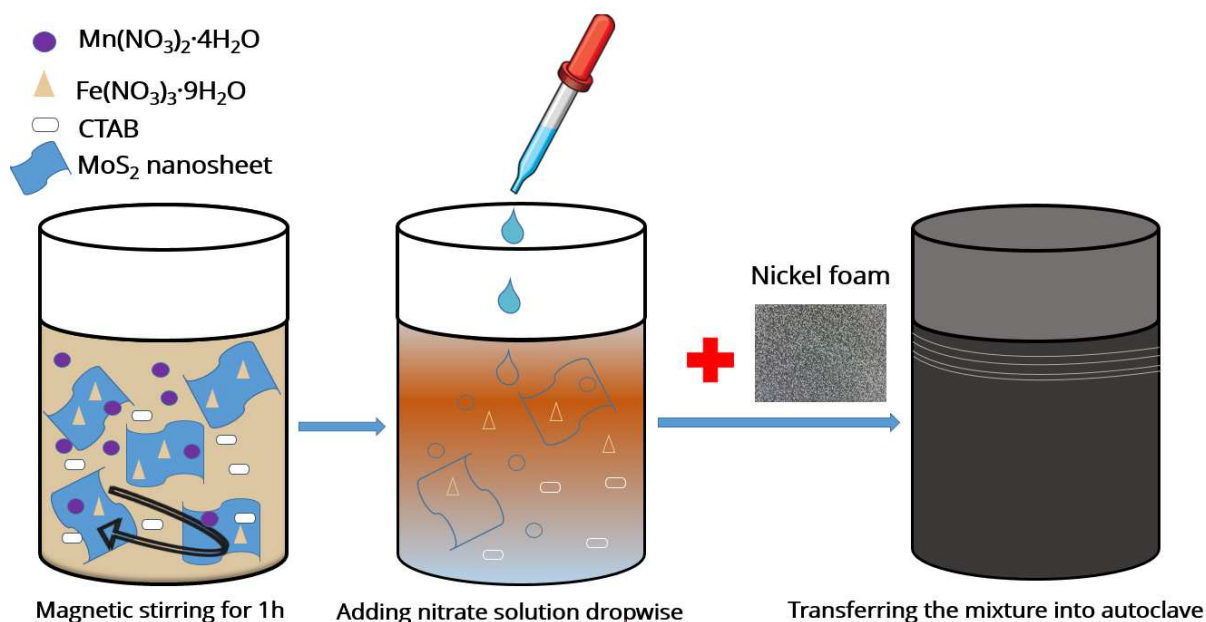


Figure 1: The procedure to synthesize the $\text{MnFe}_2\text{O}_4/\text{MoS}_2$ -coated Ni foam.

2.2. Characterization

Crystalline structures of the samples were identified using a PANalytical X'pert MPD (Philips) diffractometer with a $\text{Cu-K}\alpha$ radiation source ($\lambda = 0.15406 \text{ nm}$). Structural fingerprints of the ferrites and the MoS_2 nanosheets were investigated by a Takram P50C0R10 Raman spectrometer (Teksan Co., Iran) employing an Nd:YAG laser ($\lambda_{\text{ex}} = 532 \text{ nm}$) at room temperature. Field-emission scanning electron microscopy (FESEM) was used to observe the morphology of the samples. The optical properties of the nanocomposites were examined using a Unico 4802 UV-Vis photospectrometer.

2.3. Electrochemical tests

The supercapacitive performance of the samples was investigated using a three-electrode setup containing the coated Ni foam substrate (1 cm^2) as the working electrode, a square-shaped platinum sheet (1 cm^2 , 99.99%) as the counter electrode, and Ag/AgCl as the reference electrode in a 3 M KOH solution at room temperature. The electrochemical measurements involved cyclic voltammetry (CV), galvanostatic charging/discharging (GCD), and electrochemical impedance spectroscopy (EIS) techniques using a VSP-300 Multichannel Potentiostat/Galvanostat/EIS instrument (Bio-Logic Science Instruments). The CV measurements were recorded at different scan rates (5–100 mV/s) within the potential window of 0–0.55 V. The GCD measurements were recorded at different current densities with the potential window of 0–0.4 V.

2.4. Asymmetric two-electrode supercapacitor setup

An asymmetric two-electrode supercapacitor device was assembled by using activated carbon (AC) as the negative electrode and the $\text{MnFe}_2\text{O}_4/\text{MoS}_2$ nanocomposite as the positive electrode. The electrodes were separated by a filter paper wetted with 3 M KOH solution as the electrolyte. The AC electrode was prepared from the activated carbon and PVDF, as a binder, with the weight ratio of 95:5 dispersed in NMP. The prepared dispersion was coated on a nickel foam substrate by a brush and the obtained electrode was dried in an oven at 60°C for 10 h. The masses of the positive and negative electrodes were balanced according to the equation¹³

$$\frac{m_+}{m_-} = \frac{C_s^- \Delta V^-}{C_s^+ \Delta V^+} \quad \text{Eq. 1}$$

where m is the mass, C_s is the specific capacitance, ΔV is the potential window, and (+) and (−) denote

the positive and the negative electrodes, respectively. The coated mass on the negative electrode was ~3 mg. The CV measurements were recorded at different scan rates (5-100 mV/s) within the potential window of 0-1.5 V. The GCD measurements were recorded at different current densities with the potential window of 0-1.5 V.

2.5. Computational methods

First-principles calculations were performed in the framework of density functional theory (DFT), as implemented in the Quantum Espresso package (version 6.3) ²⁷, using the plane-wave basis set and ultrasoft pseudopotentials ²⁸. The spin polarization was included in both geometry optimizations and electronic structure calculations. The generalized gradient approximation (GGA) developed by Perdew, Burke, and Ernzerhof (PBE) ²⁹ was applied for electron exchange-correlation functionals with the on-site Coulomb repulsion U terms ³⁰ of U(Mn)=3.9 eV and U(Fe)=5.3 eV to reproduce experimental data ¹³. The kinetic energy cutoffs for wavefunctions and charge densities were set to 50 and 450 Ry, respectively. To sample the first Brillouin zone for electronic structure calculations, we adopted the k-point grid of 9×9×1 for the unit cell of the MoS₂ monolayer, 6×6×5 for the bulk MnFe₂O₄, and the k-point grid of 6×6×1 for the MnFe₂O₄/MoS₂ interface. All structures were fully relaxed until the convergence criteria of energy and force became less than 10⁻⁶ Ry and 10⁻³ Ry/Bohr, respectively. All crystal images were produced by VESTA ³¹.

3. Results and discussions

The XRD patterns of the samples are shown in Fig. 2. The XRD pattern of the bulk MoS₂ shows all the characteristic peaks corresponding to the hexagonal phase of MoS₂ with the JCPDS card No.00-037-1492. However, the XRD pattern of the exfoliated MoS₂ nanosheets shows only the (002) diffraction peak, indicating the successful exfoliation of MoS₂ into few-layer nanosheets. In the pattern of MnFe₂O₄ nanoparticles, the peaks at 2θ=18°, 30°, 35°, 43°, 53°, 57°, and 63° correspond to (111), (220), (311), (400), (422), (511), and (440), which are attributed to the cubic spinel structure of MnFe₂O₄ with the space group of *Fd3m* with the JCPDS card No. 96-591-0064 ²⁵. No other peak is seen, indicating the purity of the prepared nanoparticles. To calculate the crystallite size and the lattice strain for the MnFe₂O₄ nanoparticles, the Williamson-Hall analysis formula was applied ³²

$$\beta_{hkl} \cos \theta_{hkl} = \frac{k\lambda}{D} + 4\epsilon \sin \theta_{hkl} \quad \text{Eq. 2}$$

where θ_{hkl} is the diffraction peak angle, β_{hkl} is the full-width at half maximum of the (hkl) diffraction peak, D is the crystallite size, K is the shape factor approximated to 0.9, λ is the incident X-ray wavelength (1.5406 Å), and ϵ is the lattice strain ³³. Accordingly, D and ϵ are calculated from the Y-intercept and the slope of the line fitted on the plot of $4\sin\theta$ versus $\beta\cos\theta$, respectively ^{25,33}. Therefore, the crystallite size of the MnFe₂O₄ nanoparticles was calculated ~9.5 nm with a compressive strain of -0.0144. In the XRD pattern of the MnFe₂O₄/MoS₂-coated Ni foam, all of the peaks related to MnFe₂O₄ are seen with a peak at 2θ=14° related to few-layer MoS₂ nanosheets and two other peaks at 2θ=43° and 53° corresponding to the Ni foam substrate. This indicates that the nanocomposite has been successfully prepared.

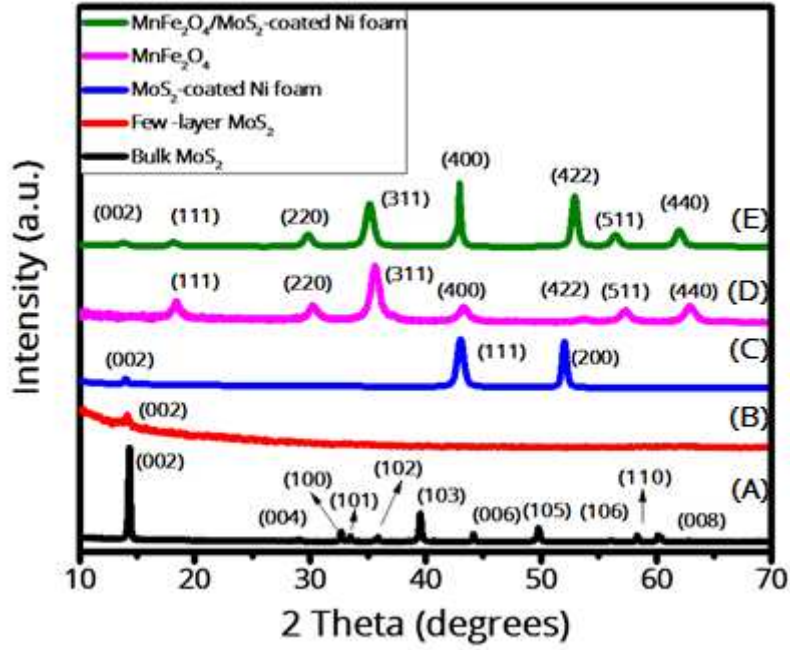


Figure 2: XRD patterns of (A) bulk MoS₂, (B) exfoliated MoS₂ nanosheets, (C) MoS₂-coated Ni foam, (D) MnFe₂O₄ nanoparticles, and (E) MnFe₂O₄/MoS₂-coated Ni foam.

Fig. 3 shows the Raman spectra of the samples. The Raman spectrum of few-layer MoS₂ nanosheets shows two peaks at 385 and 410 cm⁻¹ attributed to the in-plane (E_{2g}) and the out-of-plane (A_{1g}) vibration modes, respectively, of few-layer MoS₂²⁵. In the Raman spectrum of MnFe₂O₄ nanoparticles, the E_g band (189 cm⁻¹) is due to the asymmetric and symmetric bending of O with respect to Fe, the F_{2g}(1) band (107 cm⁻¹) is due to the translational movement of the whole tetrahedron (FeO₄), and the A_{1g} band (630 cm⁻¹) is due to the symmetric stretching of oxygen atoms along Fe-O (or Mn-O) tetrahedral bonds¹³. The bands confirm the inverse spinel structure of the MnFe₂O₄³⁴. The Raman spectrum of the MnFe₂O₄/MoS₂ nanocomposite shows the peaks due to MnFe₂O₄ and also the F_{2g}(2) band that is due to the asymmetric stretching of Fe/Mn–O bonds as well as the E_{2g} band of few-layer MoS₂ nanosheets, confirming the presence of both MnFe₂O₄ and MoS₂ in the nanocomposite. Here, the peaks due to MnFe₂O₄ have shifted toward lower wavenumber as compared to the pure ferrite nanoparticles (617, 484, 195, and 86 cm⁻¹ corresponding to A_{1g}, F_{2g}(1), E_g, and F_{2g}(2) modes, respectively).

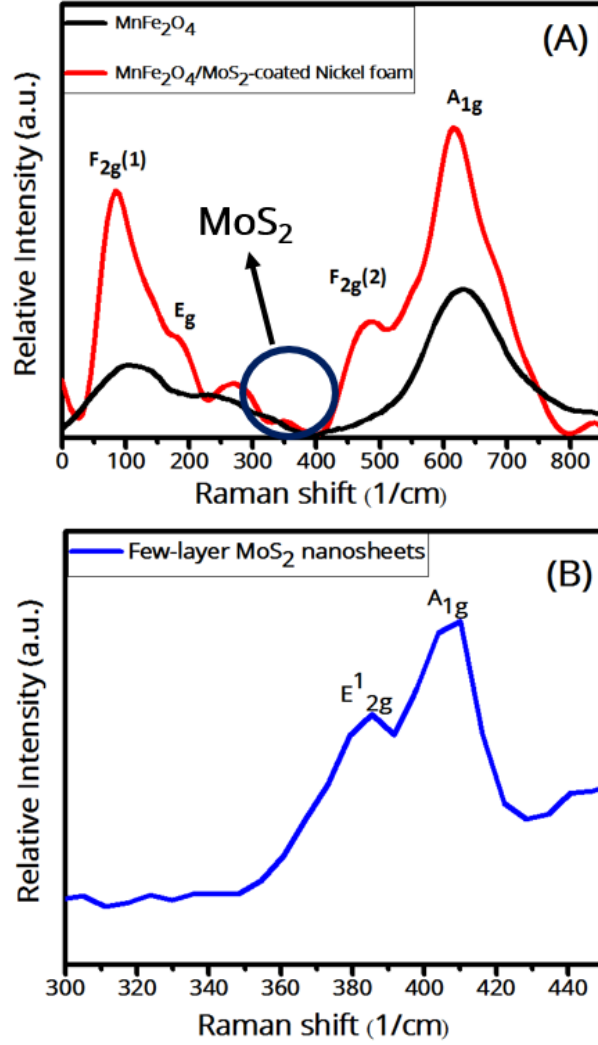


Figure 3: Raman spectra of (A) MnFe_2O_4 nanoparticles, and $\text{MnFe}_2\text{O}_4/\text{MoS}_2$ -coated Ni foam, (B) few-layer MoS_2 nanosheets.

UV-vis absorption spectroscopy is a powerful tool to investigate the optical properties of semiconductor materials³⁵. UV-Vis absorption spectra of the samples with their corresponding Tauc's plots are shown in Fig. 4. Optical bandgaps of the samples were estimated using the classical Tauc's relation

$$(\alpha h\nu)^n = B(h\nu - E_g) \quad \text{Eq. 3}$$

where α , ν , n , B , h , and E_g is the absorption coefficient, the photon frequency, a constant that depends on the bandgap type (1/2 and 2 for direct and indirect band gaps), a constant, the Planck's constant, and the optical bandgap, respectively. The optical band gap is estimated from an extrapolation of the linear part of $(\alpha h\nu)^2$ versus the photon energy ($h\nu$) for direct bandgaps. The UV-Vis spectrum of MoS_2 nanosheets shows four characteristic peaks at 684, 625, 481, and 399 nm, corresponding to four different electronic transitions denoted with A, B, C, and D, consistent with previously reported values²⁶. The few-layer MoS_2 nanosheets exhibit a bandgap of 1.7 eV, consistent with the literature²⁶. The MnFe_2O_4 sample shows a bandgap of 1.6 eV¹³. It is observed that the bandgap of the $\text{MnFe}_2\text{O}_4/\text{MoS}_2$ nanocomposite is almost smaller than that of the pure MnFe_2O_4 nanoparticles. This is due to the creation of intermediate states between the valence band and the conduction band of MnFe_2O_4 resulting from MoS_2 . The lower bandgap of the $\text{MnFe}_2\text{O}_4/\text{MoS}_2$ nanocomposite as compared to the pure MnFe_2O_4 nanoparticles and the presence of intermediate states can increase the conductivity of the nanocomposite which in turn can enhance its capacitance.

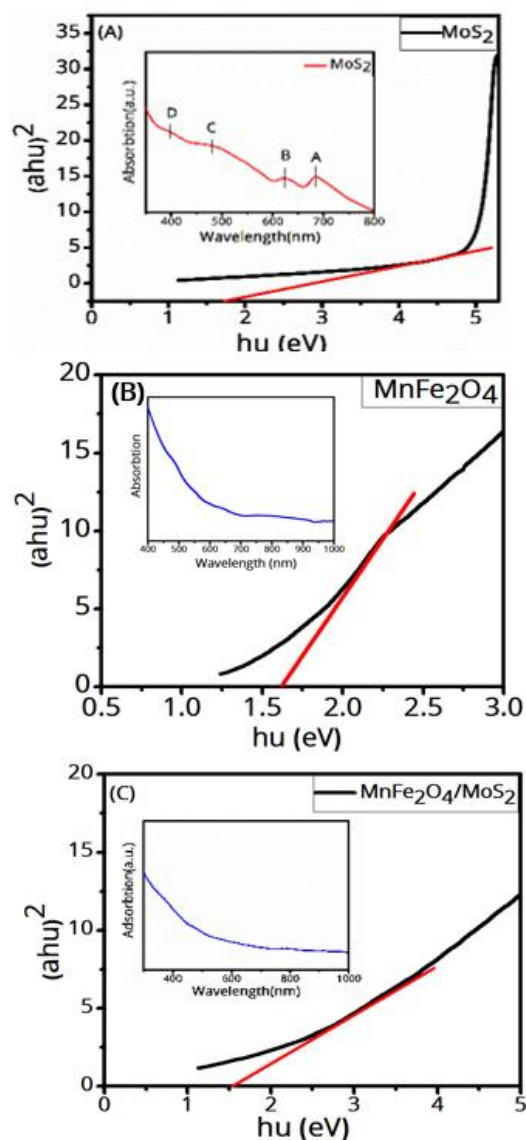


Figure 4: UV-Vis absorption spectra and Tauc plots (insets) of (A) MoS₂ nanosheets, (B) MnFe₂O₄ nanoparticles, and (C) the MnFe₂O₄/MoS₂ nanocomposite.

FESEM images of the prepared samples are shown in Fig. 5. The pure MoS₂ nanosheets in Fig. 5 (A, B) are sufficiently wide with a lateral size of about 2 to 3 μm , which is appropriate as a substrate to hold other nanoparticles. Some obvious foldings can be seen in these MoS₂ nanosheets, and one can conclude that they are few-layer. On the other hand, Fig. 5 (C, D) shows that the MoS₂ nanosheets are uniformly and densely covered with MnFe₂O₄ nanoparticles with an average size of ~ 10 nm, which is very close to the size calculated from the XRD spectrum (~ 9.5 nm). This uniform and dense distribution of the ferrite nanoparticles enabled by the presence of MoS₂ nanosheets can provide a larger surface to volume ratio, required for an enhanced charge transfer and, in turn, a higher capacitance.

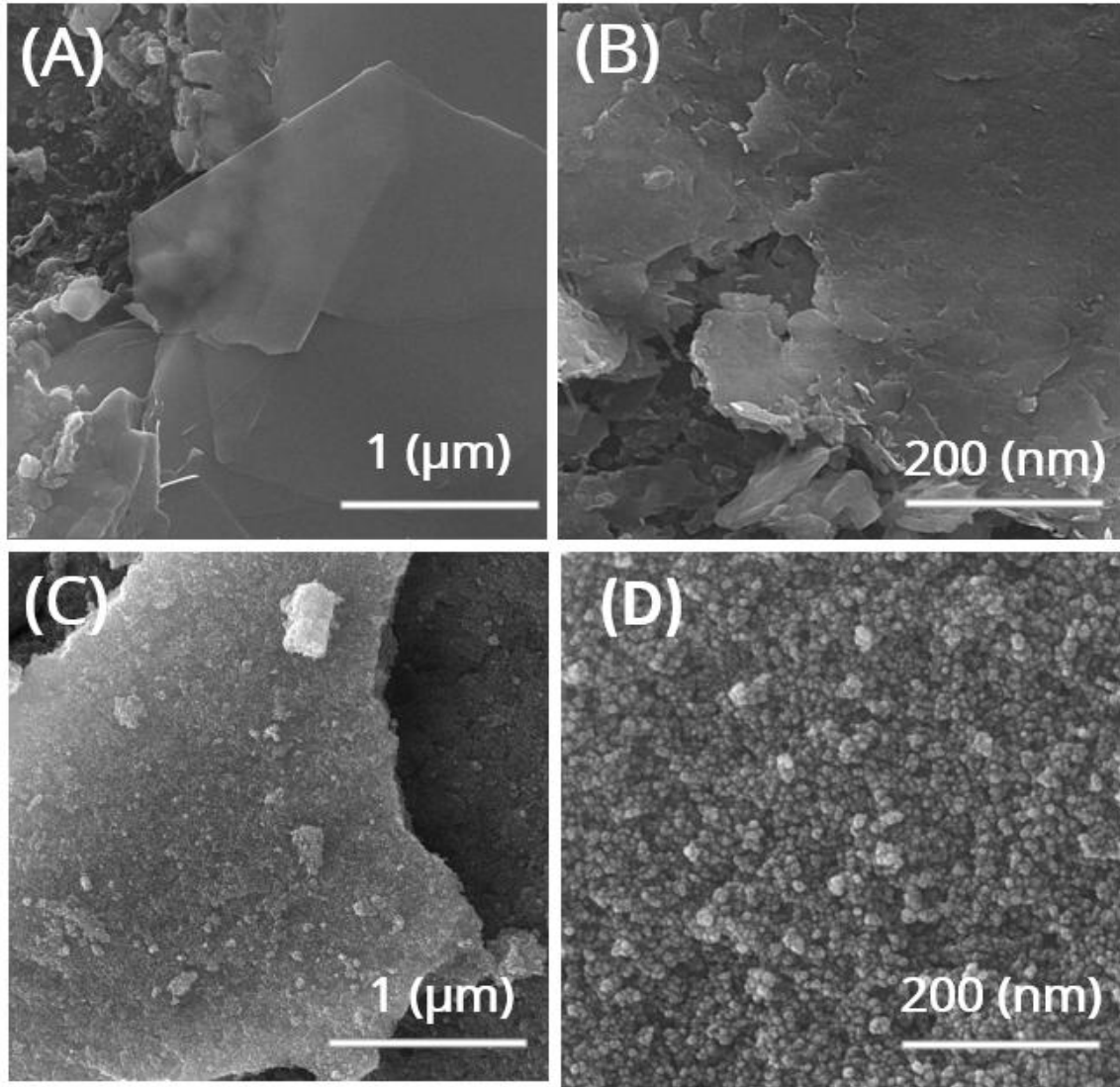


Figure 5: FESEM images of (A, B) pure MoS₂ nanosheets and (C, D) the MnFe₂O₄/MoS₂ nanocomposite

Fig. 6 shows the CV curves of the samples at various scan rates, where two peaks are seen with positive and negative currents corresponding to oxidation and reduction processes at the electrode's surface, respectively³⁶. As it is seen, by increasing the scan rate the oxidation and reduction peaks shift to higher and lower potentials, respectively, because a shorter time would be available for the electrolyte ions to access the electrode's surface. However, there is a trade-off between potential and time. Besides, at higher scan rates, both the area under the CV curve and the current increase. Nevertheless, it is seen that the area enclosed in a CV curve (or equivalently, the specific capacitance) decreases as the scan rate increases. This is because at higher scan rates, due to the fast migration of ions, some parts of the active surface areas become inaccessible for the charge storage process^{13,17,37}. Fig. 6 also represents the galvanostatic charge/discharge (GCD) curves of the samples at different current densities in a potential window of 0 to 0.4 V. It is seen that the discharge time of the samples decreases as the current density increases, explained above. The specific capacitance of the electrodes was calculated from their discharge curves according to the equation^{13,17}

$$C_{sp} = 2I \frac{\int V dt}{m (\Delta V)^2} \quad \text{Eq. 4}$$

at different current densities, where C_{sp} , I/m , $\int V dt$, and ΔV are the specific capacitance (F/g), the

current density (A/g), the area under the discharge curve, and the active potential window, respectively. The specific capacitances of the samples are reported in Table 1.

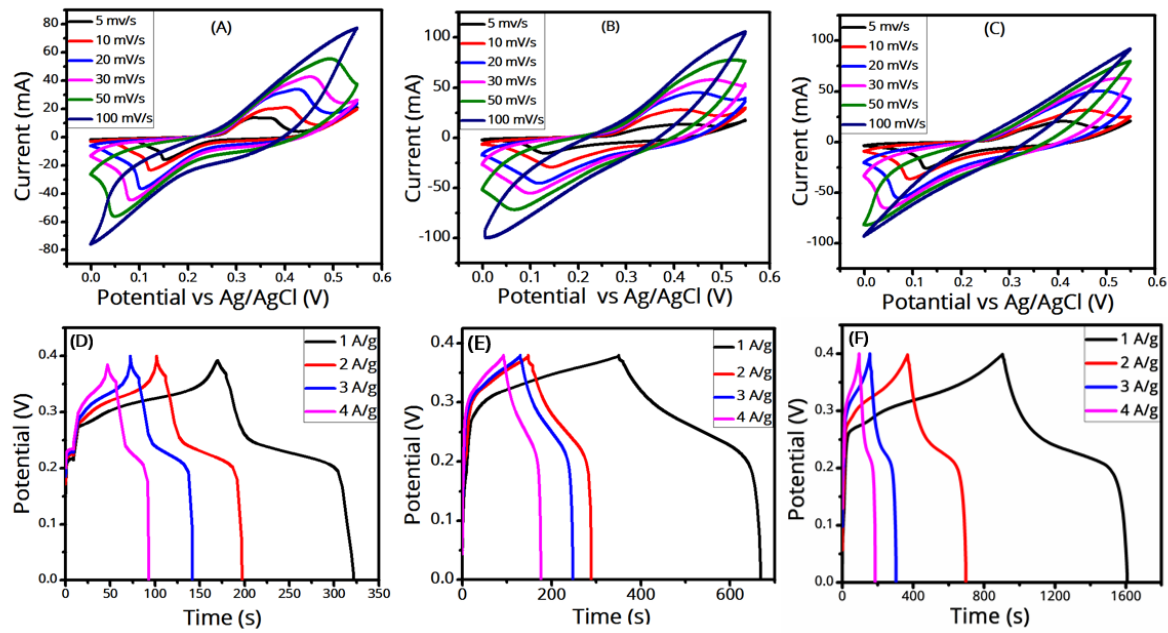


Figure 6: CV (at various scan rates) and GCD (at various current densities) curves of (A, D) few-layer MoS₂ nanosheets, (B, E) MnFe₂O₄ nanoparticles, and (C, F) the MnFe₂O₄/MoS₂ nanocomposite.

Table 1: Specific capacitance values of the samples at various current densities.

Current density (A/g)	Specific capacitance (F/g)		
	MoS ₂ nanosheets	MnFe ₂ O ₄	MnFe ₂ O ₄ /MoS ₂
1	440	600	2093
2	428	520	1982
3	415	453	1870
4	346	375	1810

As it is seen in Fig. 7 (A), which compares the GCD curves of the samples at the current density of 1 A/g, the discharge time, or equivalently the specific capacitance, of the MnFe₂O₄/MoS₂ composite is more than those of both MoS₂ and MnFe₂O₄. This can be for several reasons. Firstly, MoS₂ is itself an active material for electrochemical reactions due to its electronic structure as well as layered structure, because it can accommodate electrolyte ions in its layered structure. Secondly, due to its versatile redox states, MnFe₂O₄ has a pseudocapacitive behavior. Therefore, both MoS₂ and MnFe₂O₄ contribute to the supercapacitance of the MnFe₂O₄/MoS₂ nanocomposite. On the other hand, MoS₂ nanosheets prevent the MnFe₂O₄ from agglomeration and aggregation. Similarly, MnFe₂O₄ nanoparticles prevent the MoS₂ nanosheets from restacking. This will increase the active surface area for charge storage processes. In the next section on DFT calculations, we will see how MoS₂ can redistribute the stored charges on MnFe₂O₄ to achieve an improved capacitance. As can be seen in Fig. 7(B), the specific capacitance decreases as the current density increases, which is due to the ion diffusion mechanism. In other words, at a lower current density, the electrolyte ions have enough time to penetrate into the active sites on the electrode material, leading to a higher specific capacitance¹³. Fig. 7(C) compares the CV curves of the prepared electrodes at the scan rate of 5 mV/s. The reduction and oxidation peaks are seen around 0.14 V and 0.4 V, respectively. As it is seen, the MnFe₂O₄/MoS₂ nanocomposite shows a larger CV-enclosed area than that of MnFe₂O₄, which is itself larger than that of MoS₂. This could indicate the higher capacitance of the MnFe₂O₄/MoS₂ nanocomposite than MnFe₂O₄. The incorporation of MoS₂ nanosheets largely increased the specific capacitance of MnFe₂O₄ from 600 to 2093 F/g at 1 A/g. The

power densities of the MoS₂, MnFe₂O₄, and MnFe₂O₄/MoS₂ samples were obtained at the current density of 1 A/g, listed in Table 2, and their Ragone plots (energy density versus power density) are shown in Fig. 7(D). The energy and power densities of the samples were calculated based on

$$E = \frac{1}{2} C_{sp} \Delta v^2 \quad \text{Eq. 5}$$

$$P = \frac{E}{t} \quad \text{Eq. 6}$$

respectively, where Δv and t are the potential windows and the discharge time (h)³⁸. Cyclic stability tests were performed at the current density of 20 A/g for 2000 GCD cycles, as shown in Fig. 7(E). It is seen that the incorporation of MoS₂ nanosheets considerably improved the cycling stability of the pure MnFe₂O₄ nanoparticles. This can be due to the fact that MoS₂ prevents the MnFe₂O₄ nanoparticles from detaching from the electrode into the electrolyte, which can improve the capacitance stability of the composite. Electrochemical impedance spectroscopy (EIS) was used to analyze the resistance information of samples. The frequency range of the impedance measurements is 10mHz-100kHz. An EIS curve typically consists of two parts: (1) the high-frequency region is a semicircle and (2) the low-frequency region is a straight line, indicating the charge-transfer resistance, and an inclined line, indicating the diffusion of ions into the electrolyte^{39,40}. According to the EIS plots in Fig. 7(F), the charge transfer resistance of the samples is negligible. The internal resistance can be obtained from the slope of the curves intersecting the x-axis. According to the EIS plots, the internal resistance of the MnFe₂O₄/MoS₂ nanocomposite is lower than those of MoS₂ and MnFe₂O₄ (also see the DFT section), so it has a higher conductivity suitable for supercapacitance. To sum up, the comparative results show that the MnFe₂O₄/MoS₂ nanocomposite exhibit better capacitive performance compared to both MoS₂ and MnFe₂O₄.

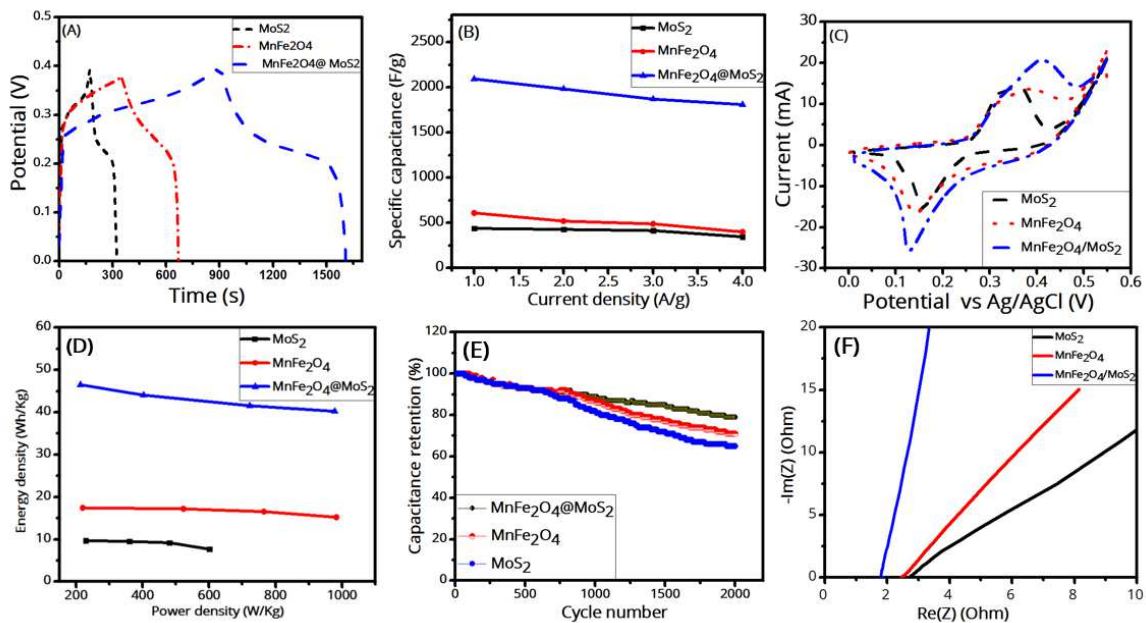


Figure 7: (A) GCD curves of the samples at the current density of 1 A/g, (B) specific capacitance versus current density for the samples, (C) CV curves of the samples at the scan rate of 5 mV/s, (D) Ragone plots (energy density versus power density) of the samples, (E) cycling stabilities of the samples during 2000 GCD cycles at the current density of 20 A/g, and (F) EIS curves of the samples.

Table 2: The calculated energy densities and power densities of the samples at the current density of 1 A/g.

Sample	Power density (W/Kg)	Energy density (Wh/Kg)
--------	----------------------	------------------------

MoS₂	229.73	9.77
MnFe₂O₄	224.23	17.43
MnFe₂O₄/MoS₂	213.64	46.51

Next, we assembled the (MnFe₂O₄/MoS₂)//AC asymmetric supercapacitor in a two-electrode setup, as discussed in the “Experimental” section. Fig. 8(A) shows the CV curves of the device for incremental voltages to confirm its operating potential. It is seen that the capacity increases as the potential window increases, indicating the ability of the device to perform faradaic processes at higher voltages. Fig. 8(B) shows the CV curves of the device for various scan rates at the potential window of 0-1.5 V, showing quasi-rectangular shapes that illustrate the good electrochemical reversibility of the device. Fig. 8(C) shows the GCD curves of the device for various current densities. The charge and discharge parts of the GCD curves are almost symmetric, which demonstrates a small internal resistance drop, indicating the contributions from both the faradaic processes and the double layer capacitance⁴¹. Fig. 8(D) illustrates the lighting up of a green light-emitting diode (LED) using the (MnFe₂O₄/MoS₂)//AC asymmetric supercapacitor.

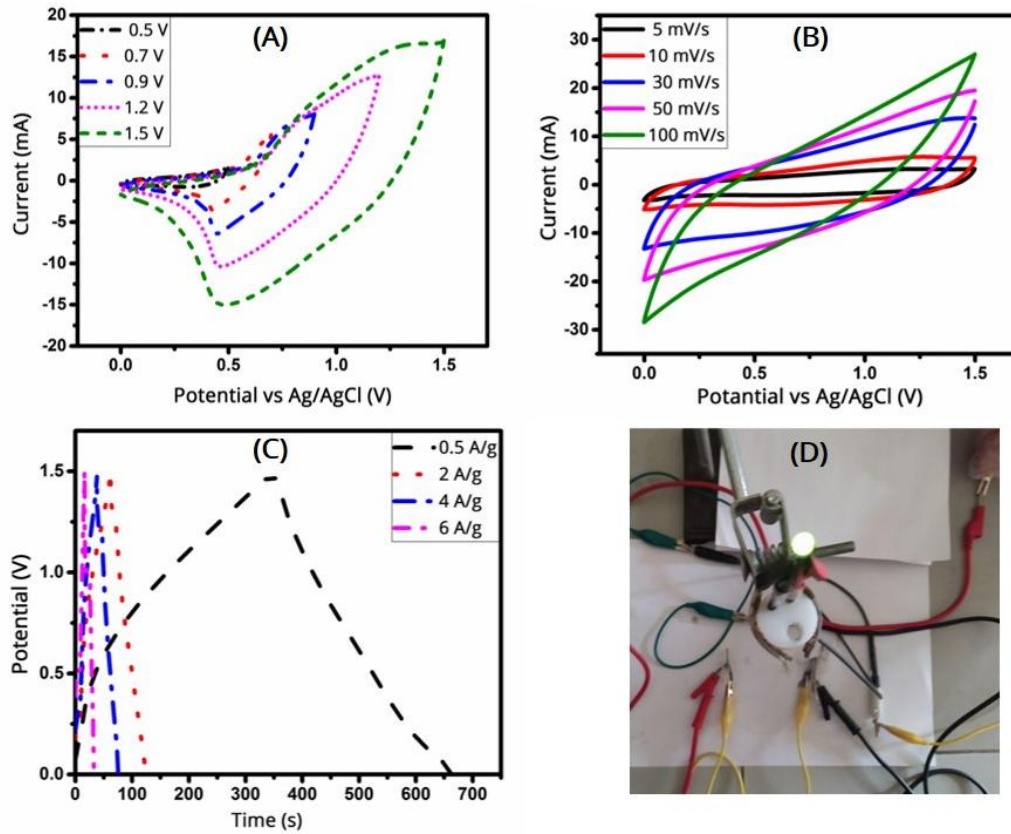


Figure 8: CV curves of the (MnFe₂O₄/MoS₂)//AC asymmetric supercapacitor (A) for different potential windows at 20 mV/s and (B) for different scan rates at the potential window of 1.5 V. (C) GCD curves of the supercapacitor at different current densities at the potential window of 1.5 V. (D) A picture of the assembled asymmetric supercapacitor lighting up a green LED.

4. DFT study

MoS₂ is a layered transition metal dichalcogenide where its layers are bound together by weak van der Waals (vdW) forces. Each MoS₂ monolayer consists of three atomic layers in the sequence of S-Mo-S. Bulk MoS₂ is a p-type indirect-bandgap semiconductor (1.23 eV), and its bandgap slightly increases to 1.8 eV as the number of layers decreases to one^{42,43}. Fig. 9(A) shows top and side views of the optimized

structure of the MoS₂ monolayer and its atom-projected density of states. We found the optimized lattice constant of 3.18 Å and the Mo-S bond length of 2.41 Å, and the MoS₂ monolayer shows a direct bandgap of 1.76 eV at the K point, consistent with ⁴³. On the other hand, MnFe₂O₄ is an insulating, soft ferrimagnetic spinel ferrite, which crystallizes in a mixed-phase spinel structure ⁴⁴ with an almost low inversion degree of 0.2, where 80% and 20% of Mn²⁺ ions occupy the tetrahedral sites and octahedral sites, respectively, and Mn²⁺ and Fe³⁺ ions are distributed in the remaining tetrahedral and octahedral sites. Recently, we compared the experimental and theoretical results of MnFe₂O₄ and showed that the true XRD pattern of MnFe₂O₄ is a combination of normal and inverse spinel XRD patterns ¹³. However, for the sake of simplicity, we considered here the normal spinel configuration for MnFe₂O₄ (see Fig. 9(B)). We considered a 28-atom unit cell for the bulk MnFe₂O₄ as half of a simple cubic structure. Fig. 9(B) shows the unit cell and the atom-projected density of states of the bulk MnFe₂O₄. It is seen that the structure is an insulator with a direct bandgap of 1.41 eV. The a and c lattice constants were found 6.14 and 8.68 Å, respectively.

Next, we created the MnFe₂O₄/MoS₂ interface (see Fig. 9(C)). The lattice mismatch between the MnFe₂O₄ surface and the MoS₂ monolayer was ~5%. We applied the strain to the MoS₂ monolayer because it only affects its bandgap and can not change its semiconducting nature ⁴⁵. In the optimized structure, the smallest distance between Mn and S atoms is 2.79 Å, which is larger than the sum of the covalent radii of both atoms (1.39 and 1.02 Å for Mn and S, respectively), indicating that the coupling between the MnFe₂O₄ slab and the MoS₂ monolayer is of the vdW type, not covalent. The binding energy between the MoS₂ monolayer and the MnFe₂O₄ slab is defined as:

$$E_b = E_{interface} - E_{MnFe_2O_4} - E_{MoS_2} \quad \text{Eq. 7}$$

where E_b is the binding energy and $E_{MnFe_2O_4}$, E_{MoS_2} , and $E_{interface}$ are the total energies of the MnFe₂O₄/MoS₂ interface, the MoS₂ monolayer, and the MnFe₂O₄ slab, respectively. The binding energy (E_b) was calculated -1.44 eV per unit cell, indicating the physisorption nature of the coupling between the MnFe₂O₄ slab and the MoS₂ monolayer. The interlayer distance of 3.19 Å confirms again the vdW nature of the coupling between the individual layers. This indicates that the MoS₂ monolayer would not have any significant influence on the electronic properties of MnFe₂O₄ and just creates some energy levels near its Fermi level and redistributes the charge density of MnFe₂O₄ at its surface.

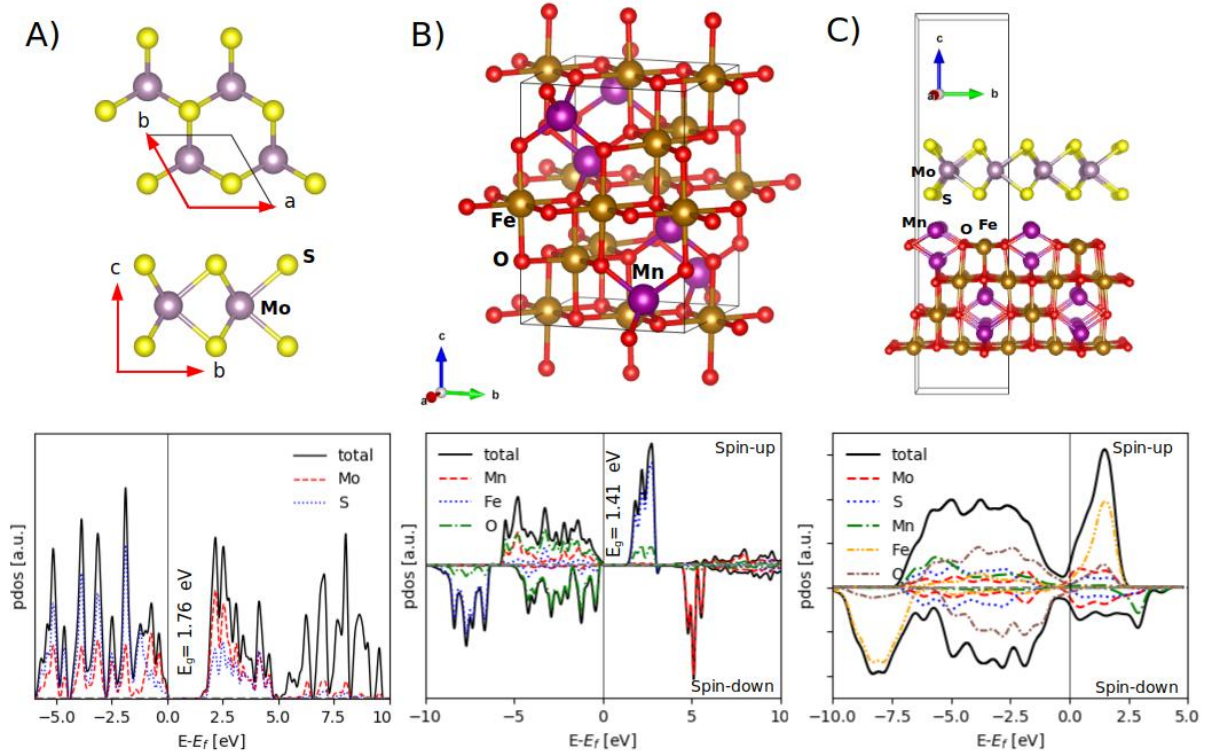


Figure 9: The unit cells and the atom-projected density of states of (A) the MoS₂ monolayer, (B) the normal spinel MnFe₂O₄, and (C) the MnFe₂O₄/MoS₂ interface.

Fig. 10(A) shows the differential charge density of the MnFe₂O₄/MoS₂ interface (i.e., the charge density of the MnFe₂O₄/MoS₂ interface minus those of the isolated MnFe₂O₄ slab and the isolated MoS₂ monolayer). It is seen that the electrons just below the MnFe₂O₄ surface have been depleted, while they have been accumulated on the MoS₂ surface, more on the nearest sulfur layer, which is due to the higher electron affinity of S as compared to Mo. The integrated charge density difference was calculated using the following equation:

$$\Delta\rho(z) = \int \rho_{interface} dx dy - \int \rho_{MnFe_2O_4} dx dy - \int \rho_{MoS_2} dx dy \quad \text{Eq. 8}$$

where $\rho_{interface}$, $\rho_{MnFe_2O_4}$, and ρ_{MoS_2} denote the charge densities corresponding to the MnFe₂O₄/MoS₂ interface, the MnFe₂O₄ slab, and the MoS₂ monolayer. The result is shown in Fig. 10(B). The net charge transfer from the MnFe₂O₄ slab to the MoS₂ monolayer was calculated as 2 electrons. Fig. 10(C) shows the in-plane averaged electrostatic potential of the MnFe₂O₄/MoS₂ interface along the z-direction. It is seen that the interface develops a very large difference (16.53 eV) in the in-plane averaged electrostatic potential across the interface, leading to a large intrinsic built-in electric field (E_{in}) from MoS₂ to MnFe₂O₄. This large built-in electric field drives electrons from MnFe₂O₄ towards MoS₂, enhancing the interlayer coupling. The attraction of charge density from MnFe₂O₄ to MoS₂ would help to enhance the charge storage of the composite. When charging, due to the constant transfer of electrons from the electrolyte to MnFe₂O₄ and in turn to MoS₂, a longer time would be needed to reach the charge saturation state (as seen in GCD curves in Fig. 7). When discharging, the process is reversed and a long time would be needed for a fully discharged state (again consistent with GCD curves in Fig. 7). This can enhance the specific capacitance of the pure MnFe₂O₄.

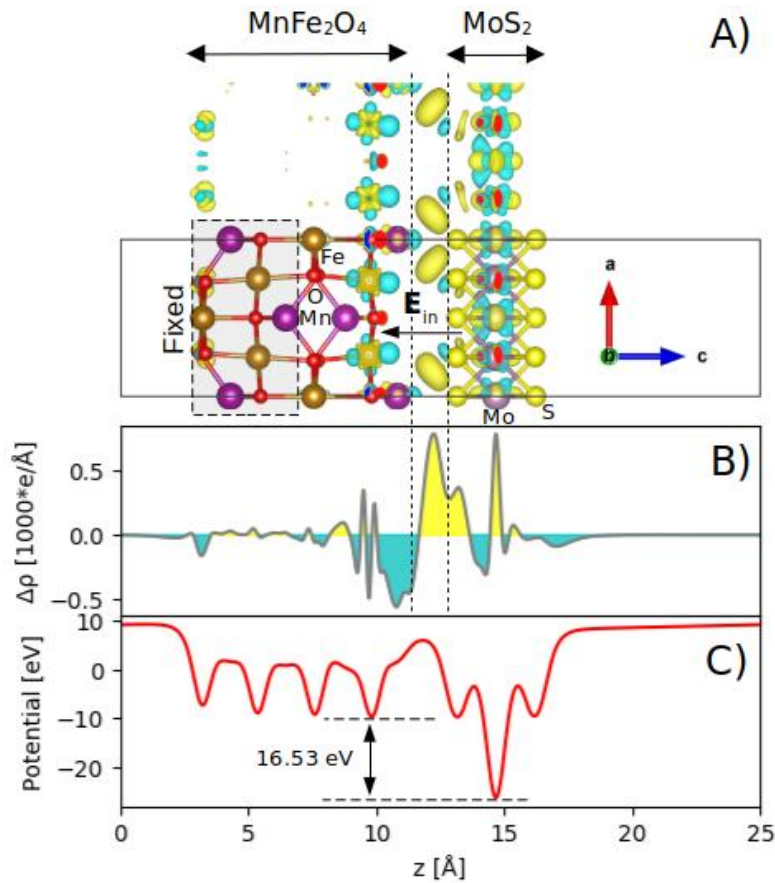


Figure 10: (Color online) (A) A 3D picture of the differential charge density of the MnFe₂O₄/MoS₂ interface, where the yellow and blue areas denote the gain and the loss of electrons, respectively, with the isosurface value of 0.016 e/Å³, with (B) its corresponding in-plane averaged differential charge density along the z-direction. The space between the dashed lines contains no atom. (C) The in-plane averaged electrostatic potential of the MnFe₂O₄/MoS₂ interface.

To sum up, according to the hybrid experimental and computational work, one can conclude that MoS₂ can enhance the charge storage capability and the specific capacitance of MnFe₂O₄ for several reasons: (1) MoS₂ itself can exhibit a supercapacitance behavior, (2) MoS₂ nanosheets will act as a substrate to hold MnFe₂O₄ nanoparticles uniformly so that they will not be agglomerated, (3) in a similar manner, the MnFe₂O₄ nanoparticles can prevent the MoS₂ nanosheets from restacking, (4) MoS₂ nanosheets provides a significantly higher active surface area, (5) MoS₂ would create several energy levels near the Fermi energy of MnFe₂O₄ that is suitable for charge storage, and (6) MoS₂ will attract the charge density of MnFe₂O₄, which can constantly redistribute the stored charges. These all can synergistically enhance the specific capacitance of pure MnFe₂O₄ nanoparticles.

5. Conclusions

MnFe₂O₄ nanoparticles were in-situ synthesized on pre-exfoliated few-layer MoS₂ nanosheets via a simple hydrothermal method, and the synthesized MnFe₂O₄/MoS₂ nanocomposite was studied for supercapacitor applications. We found that owing to the effect of MoS₂, the MnFe₂O₄/MoS₂ nanocomposite demonstrates a considerably higher (~3.5 times) specific capacitance and better charge-discharge cycling stability as compared to pure MnFe₂O₄. Using DFT calculations, we attributed the improvement to the energy levels of MoS₂ near the Fermi level of the composite, making it a conductor, and the attraction of electron charge density from MnFe₂O₄ to MoS₂, which will help the redistribution of electrons between MoS₂ and MnFe₂O₄ when charging and discharging.

References

1. Chen, T.-Y. & Lin, L.-Y. Morphology variation for the nickel cobalt molybdenum copper oxide with different metal ratios and their application on energy storage. *Electrochimica Acta* vol. 298 745–755 (2019).
2. Huang, Y.-Y. & Lin, L.-Y. Synthesis of Ternary Metal Oxides for Battery-Supercapacitor Hybrid Devices: Influences of Metal Species on Redox Reaction and Electrical Conductivity. *ACS Applied Energy Materials* vol. 1 2979–2990 (2018).
3. Liu, C., Neale, Z. G. & Cao, G. Understanding electrochemical potentials of cathode materials in rechargeable batteries. *Materials Today* vol. 19 109–123 (2016).
4. Rahimi, K. Electric-field- and strain-induced adjustability of vdW heterostructure of g-ZnO/2H-TiS₂ for optoelectronic applications. *Materials Letters* vol. 282 128680 (2021).
5. Rahimi, K. Tunable electronic properties of the novel g-ZnO/1T-TiS₂ vdW heterostructure by electric field and strain: crossovers in bandgap and band alignment types. *Physical Chemistry Chemical Physics* vol. 22 7412–7420 (2020).
6. Rahimi, K. & Yazdani, A. Incremental photocatalytic reduction of graphene oxide on vertical ZnO nanorods for ultraviolet sensing. *Materials Letters* vol. 262 127078 (2020).
7. Khan, K. *et al.* Recent developments in emerging two-dimensional materials and their applications. *Journal of Materials Chemistry C* vol. 8 387–440 (2020).
8. Kumar, P. *et al.* Review—Two-Dimensional Layered Materials for Energy Storage Applications. *ECS J. Solid State Sci. Technol.* **5**, Q3021–Q3025 (2016).
9. Lin, L. *et al.* Two-dimensional transition metal dichalcogenides in supercapacitors and secondary batteries. *Energy Storage Materials* vol. 19 408–423 (2019).
10. Chia, X., Ambrosi, A., Lazar, P., Sofer, Z. & Pumera, M. Electrocatalysis of layered Group 5 metallic transition metal dichalcogenides (MX₂, M = V, Nb, and Ta; X = S, Se, and Te). *Journal of Materials Chemistry A* vol. 4 14241–14253 (2016).
11. Pumera, M., Sofer, Z. & Ambrosi, A. Layered transition metal dichalcogenides for

- electrochemical energy generation and storage. *J. Mater. Chem. A* vol. 2 8981–8987 (2014).
12. Shi, L. & Zhao, T. Recent advances in inorganic 2D materials and their applications in lithium and sodium batteries. *Journal of Materials Chemistry A* vol. 5 3735–3758 (2017).
13. Sharifi, S., Yazdani, A. & Rahimi, K. Incremental substitution of Ni with Mn in NiFe₂O₄ to largely enhance its supercapacitance properties. *Scientific Reports* vol. 10 (2020).
14. Sharifi, S., Yazdani, A. & Rahimi, K. Effect of Co₂ content on supercapacitance properties of hydrothermally synthesized Ni_{1-x}Co_xFe₂O₄ nanoparticles. *Materials Science in Semiconductor Processing* vol. 108 104902 (2020).
15. Fu, W., Xu, X., Wang, W., Shen, J. & Ye, M. In-Situ Growth of NiFe₂O₄/2D MoS₂ p-n Heterojunction Immobilizing Palladium Nanoparticles for Enhanced Visible-Light Photocatalytic Activities. *ACS Sustainable Chemistry & Engineering* vol. 6 8935–8944 (2018).
16. Kubakaddi, S. S. Large power dissipation of hot Dirac fermions in twisted bilayer graphene. *J. Phys. Condens. Matter* (2020) doi:10.1088/1361-648X/abd526.
17. Moosavifard, S. E., Najafi, F., Izadi, M., Gharibzadeh, Z. & Habibi, Z. Facile synthesis of nanoporous spinel nickel-manganese-cobalt ternary oxide hollow spheres as high-performance supercapacitor electrode material. *Advances in Nanochemistry* **2**, 7–10 (2020).
18. Zeng, D. *et al.* Enhanced hydrogen production performance through controllable redox exsolution within CoFeAlO_x spinel oxygen carrier materials. *Journal of Materials Chemistry A* vol. 6 11306–11316 (2018).
19. Yan, Y. *et al.* Bifunctional nickel ferrite-decorated carbon nanotube arrays as free-standing air electrode for rechargeable Zn–air batteries. *Journal of Materials Chemistry A* vol. 8 5070–5077 (2020).
20. Su, L. *et al.* Sprinkling MnFe₂O₄ quantum dots on nitrogen-doped graphene sheets: the formation mechanism and application for high-performance supercapacitor electrodes. *Journal of Materials Chemistry A* vol. 6 9997–10007 (2018).
21. Zhang, Z. *et al.* Layer-stacked cobalt ferrite (CoFe₂O₄) mesoporous platelets for high-performance lithium ion battery anodes. *Journal of Materials Chemistry A* vol. 3 6990–6997 (2015).
22. Mohammadi, A., Moosavifard, S. E., Tabrizi, A. G., Abdi, M. M. & Karimi, G. Nanoporous CuCo₂S₄ Microspheres: A Novel Positive Electrode for High-Performance Hybrid Energy Storage Devices. *ACS Applied Energy Materials* vol. 2 627–635 (2019).
23. Wang, G. *et al.* Controlled synthesis of CoFe₂O₄/MoS₂ nanocomposites with excellent sedimentation stability for magnetorheological fluid. *Journal of Industrial and Engineering Chemistry* vol. 70 439–446 (2019).
24. Zeng, Y. *et al.* Fabrication of Z-scheme magnetic MoS₂/CoFe₂O₄ nanocomposites with highly efficient photocatalytic activity. *Journal of Colloid and Interface Science* vol. 514 664–674 (2018).
25. Zhao, Y. *et al.* Facile preparation of NiFe₂O₄/MoS₂ composite material with synergistic effect for high performance supercapacitor. *Journal of Alloys and Compounds* vol. 726 608–617 (2017).
26. Dong, L. *et al.* Spontaneous exfoliation and tailoring of MoS₂ in mixed solvents. *Chem. Commun.* **50**, 15936–15939 (2014).
27. Giannozzi, P. *et al.* QUANTUM ESPRESSO: a modular and open-source software project for quantum simulations of materials. *J. Phys. Condens. Matter* **21**, 395502 (2009).
28. Vanderbilt, D. Soft self-consistent pseudopotentials in a generalized eigenvalue formalism. *Physical Review B* vol. 41 7892–7895 (1990).
29. Perdew, J. P., Burke, K. & Ernzerhof, M. Generalized Gradient Approximation Made Simple [Phys. Rev. Lett. 77, 3865 (1996)]. *Physical Review Letters* vol. 78 1396–1396 (1997).
30. Cococcioni, M. & de Gironcoli, S. Linear response approach to the calculation of the effective interaction parameters in the LDA U method. *Physical Review B* vol. 71 (2005).
31. Momma, K. & Izumi, F. VESTA 3 for three-dimensional visualization of crystal, volumetric and morphology data. *Journal of Applied Crystallography* vol. 44 1272–1276 (2011).
32. Prabhu, Y. T., Rao, K. V., Kumar, V. S. S. & Kumari, B. S. X-Ray Analysis by Williamson-Hall and Size-Strain Plot Methods of ZnO Nanoparticles with Fuel Variation. *World Journal of Nano Science and Engineering* vol. 04 21–28 (2014).

33. Hussein, Hussein, H. & Yazdani, A. Investigation the influence of Fe (III) doping in Cu₂ZnSnS₄ semiconductor: Structural, optical and magnetic properties. *Optik* vol. 179 505–513 (2019).
34. Ulpe, A. C. *et al.* Photoelectrochemistry of Ferrites: Theoretical Predictions vs. Experimental Results. *Zeitschrift für Physikalische Chemie* vol. 234 719–776 (2020).
35. Ren, B., Shen, W., Li, L., Wu, S. & Wang, W. 3D CoFe₂O₄ nanorod/flower-like MoS₂ nanosheet heterojunctions as recyclable visible light-driven photocatalysts for the degradation of organic dyes. *Applied Surface Science* vol. 447 711–723 (2018).
36. Pak, M., Moshaii, A., Siampour, H., Abbasian, S. & Nikkhah, M. Cobalt-copper bimetallic nanostructures prepared by glancing angle deposition for non-enzymatic voltammetric determination of glucose. *Mikrochim. Acta* **187**, 276 (2020).
37. Eskandari, M., Malekfar, R., Buceta, D. & Taboada, P. NiCo₂O₄-based nanostructured composites for high-performance pseudocapacitor electrodes. *Colloids and Surfaces A: Physicochemical and Engineering Aspects* vol. 584 124039 (2020).
38. Bhujun, B., Tan, M. T. T. & Shanmugam, A. S. Study of mixed ternary transition metal ferrites as potential electrodes for supercapacitor applications. *Results in Physics* vol. 7 345–353 (2017).
39. Wang, H. *et al.* Preparation and performance of PANI/RFC/rGO composite electrode materials for supercapacitors. *Ionics* vol. 26 4031–4038 (2020).
40. Jeyaranjan, A., Sakthivel, T. S., Neal, C. J. & Seal, S. Scalable ternary hierarchical microspheres composed of PANI/ rGO/CeO₂ for high performance supercapacitor applications. *Carbon* vol. 151 192–202 (2019).
41. Huang, K.-J. *et al.* Layered MoS₂–graphene composites for supercapacitor applications with enhanced capacitive performance. *International Journal of Hydrogen Energy* vol. 38 14027–14034 (2013).
42. Kobayashi, K. & Yamauchi, J. Electronic structure and scanning-tunneling-microscopy image of molybdenum dichalcogenide surfaces. *Phys. Rev. B Condens. Matter* **51**, 17085–17095 (1995).
43. Yun, W. S., Han, S. W., Hong, S. C., Kim, I. G. & Lee, J. D. Thickness and strain effects on electronic structures of transition metal dichalcogenides: 2H-MX₂semiconductors (M=Mo, W; X=S, Se, Te). *Physical Review B* vol. 85 (2012).
44. Szotek, Z. *et al.* Electronic structures of normal and inverse spinel ferrites from first principles. *Physical Review B* vol. 74 (2006).
45. Lu, P., Wu, X., Guo, W. & Zeng, X. C. Strain-dependent electronic and magnetic properties of MoS₂ monolayer, bilayer, nanoribbons and nanotubes. *Physical Chemistry Chemical Physics* vol. 14 13035 (2012).

Acknowledgements

The authors would like to thank the Research Council of Tarbiat Modares University for financial support.

Author contributions

S.S. and K.R. wrote the manuscript text. K.R. performed DFT simulations. A.Y. supervised the project.

Competing interest

The authors declare no competing interests.

Data availability

The datasets generated during and/or analyzed during the current study are available from the corresponding author on reasonable requests.

Additional information

Correspondence and requests for materials should be addressed to A.Y.

Figures

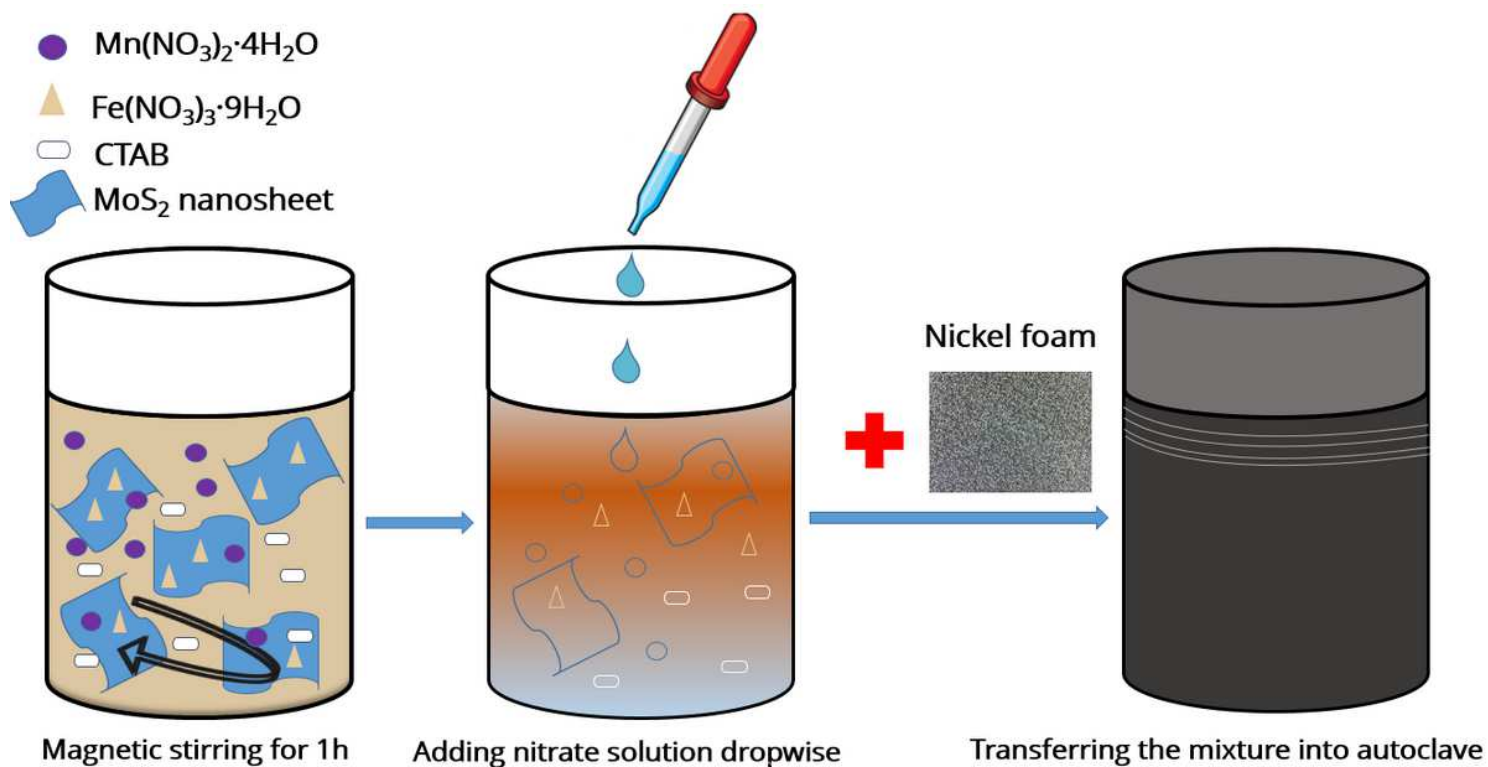


Figure 1

The procedure to synthesize the $\text{MnFe}_2\text{O}_4/\text{MoS}_2$ -coated Ni foam.

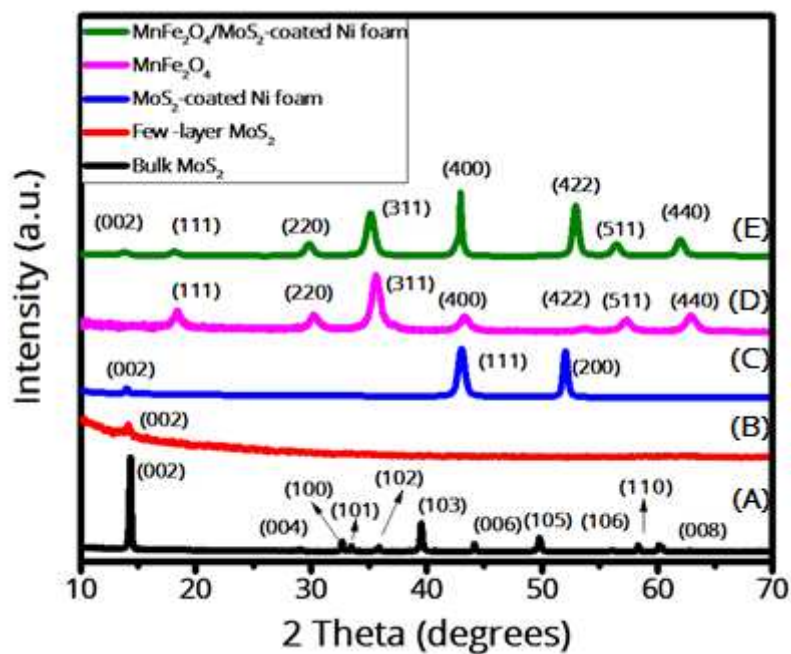


Figure 2

XRD patterns of (A) bulk MoS₂, (B) exfoliated MoS₂ nanosheets, (C) MoS₂-coated Ni foam, (D) MnFe₂O₄ nanoparticles, and (E) MnFe₂O₄/MoS₂-coated Ni foam.

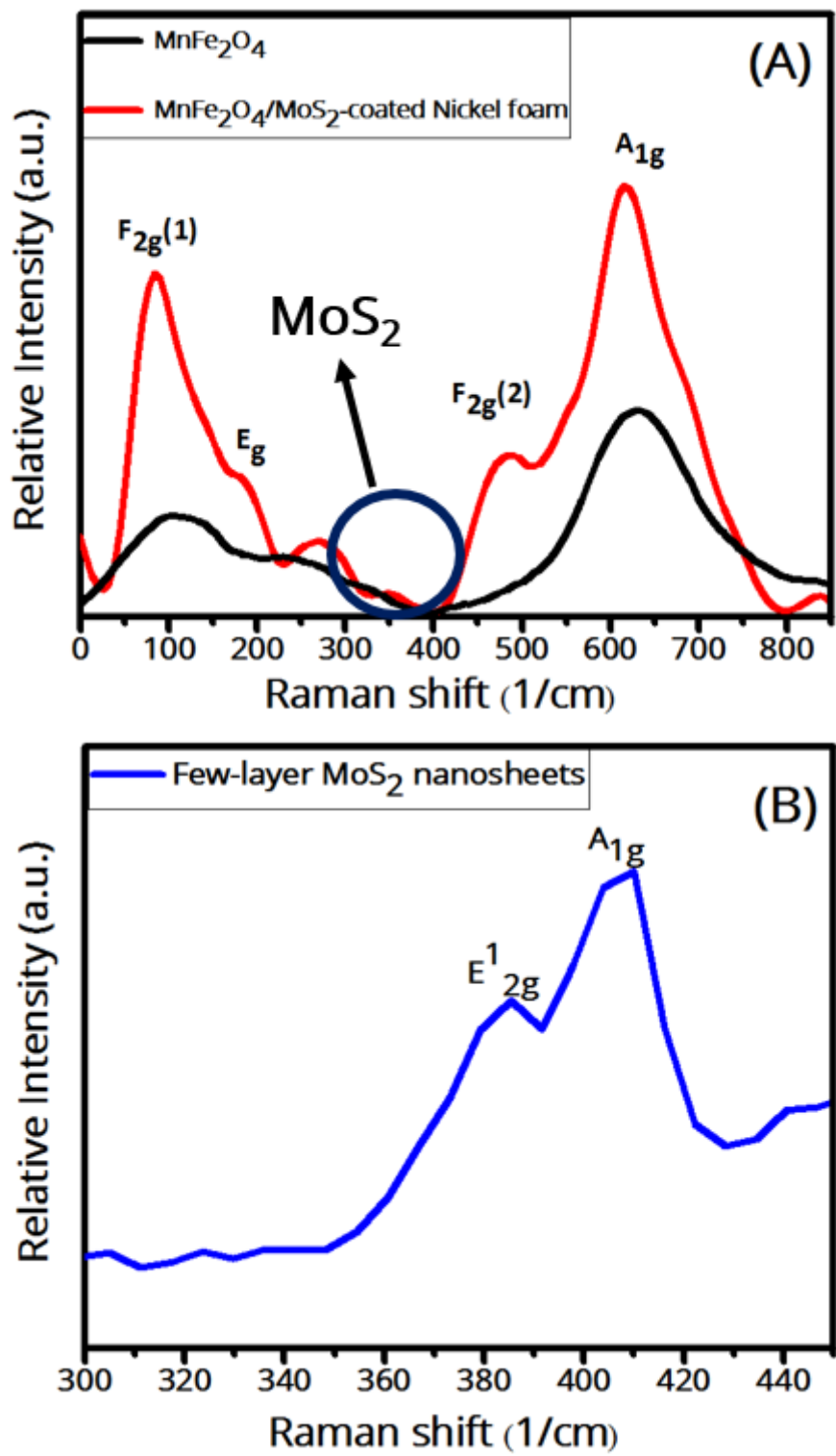


Figure 3

Raman spectra of (A) MnFe₂O₄ nanoparticles, and MnFe₂O₄/MoS₂-coated Ni foam, (B) few-layer MoS₂ nanosheets.

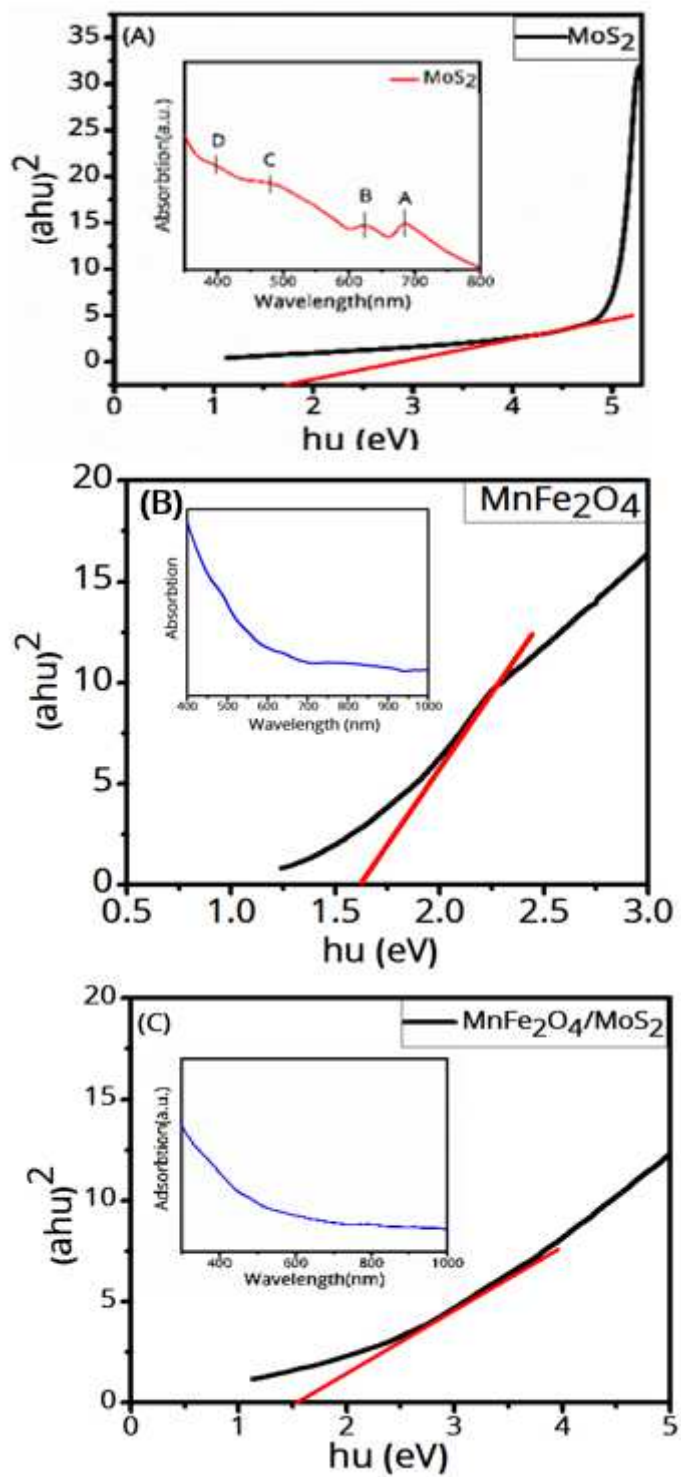


Figure 4

UV-Vis absorption spectra and Tauc plots (insets) of (A) MoS₂ nanosheets, (B) MnFe₂O₄ nanoparticles, and (C) the MnFe₂O₄/MoS₂ nanocomposite.

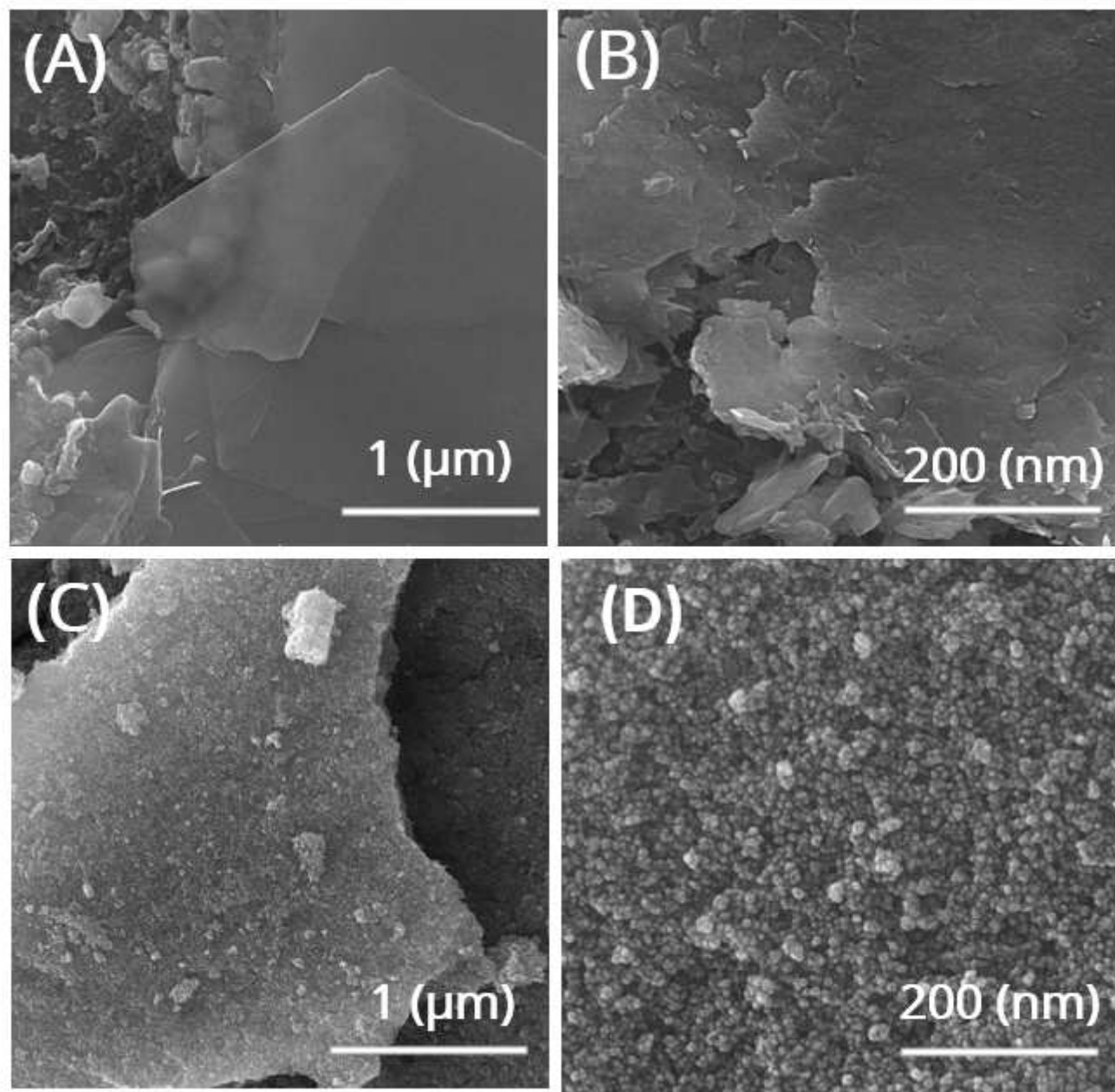


Figure 5

FESEM images of (A, B) pure MoS₂ nanosheets and (C, D) the MnFe₂O₄/MoS₂ nanocomposite

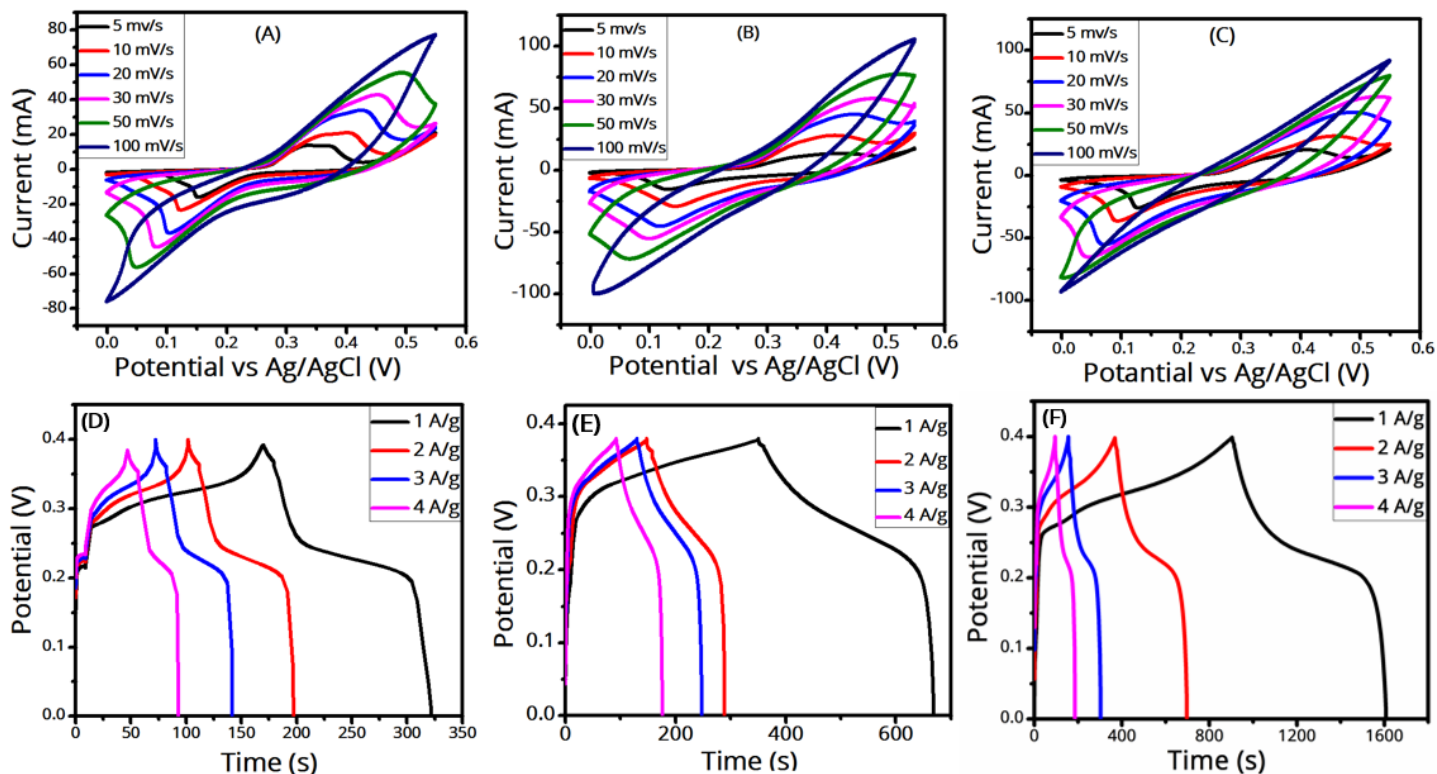


Figure 6

CV (at various scan rates) and GCD (at various current densities) curves of (A, D) few-layer MoS₂ nanosheets, (B, E) MnFe₂O₄ nanoparticles, and (C, F) the MnFe₂O₄/MoS₂ nanocomposite.

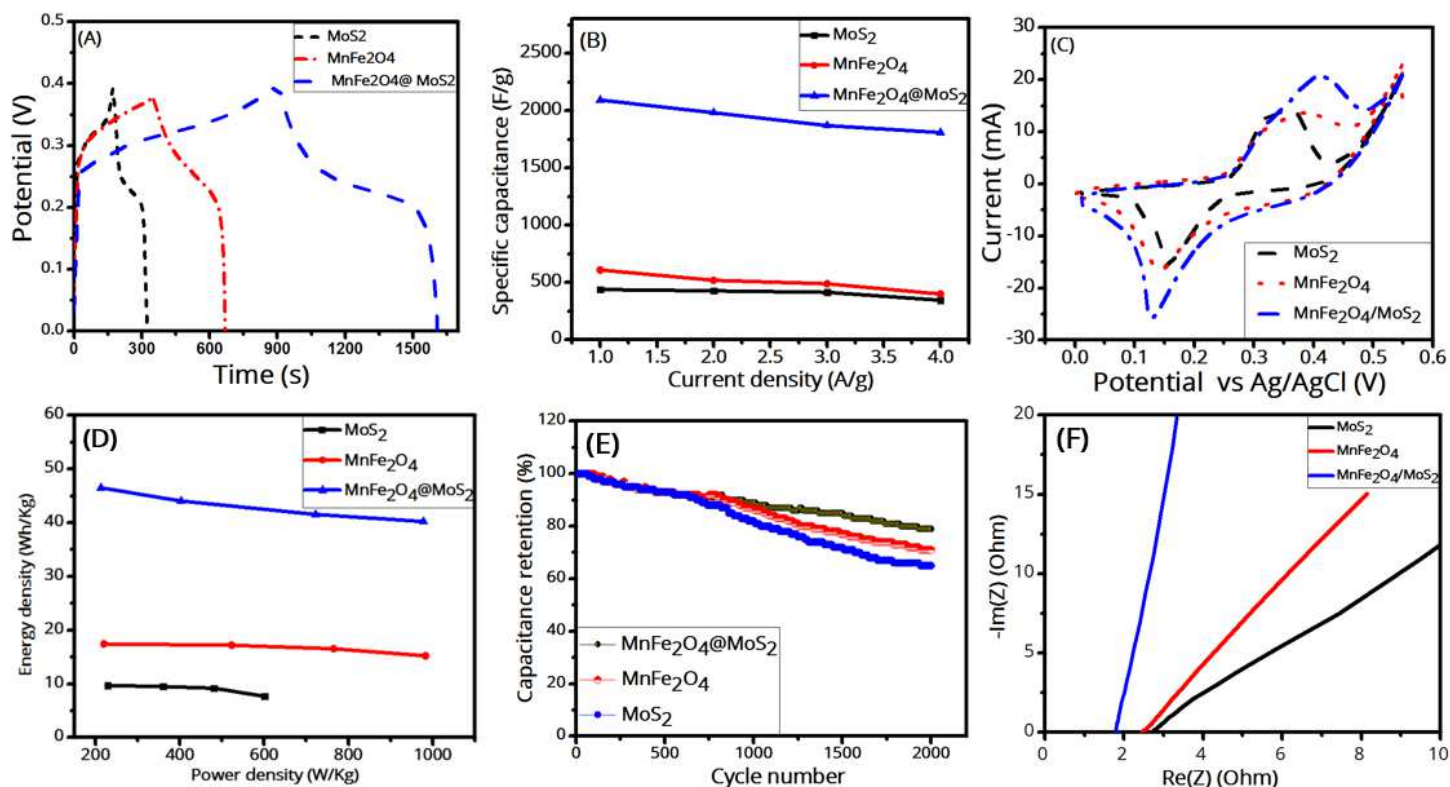


Figure 7

(A) GCD curves of the samples at the current density of 1 A/g, (B) specific capacitance versus current density for the samples, (C) CV curves of the samples at the scan rate of 5 mV/s, (D) Ragone plots (energy density versus power density) of the samples, (E) cycling stabilities of the samples during 2000 GCD cycles at the current density of 20 A/g, and (F) EIS curves of the samples.

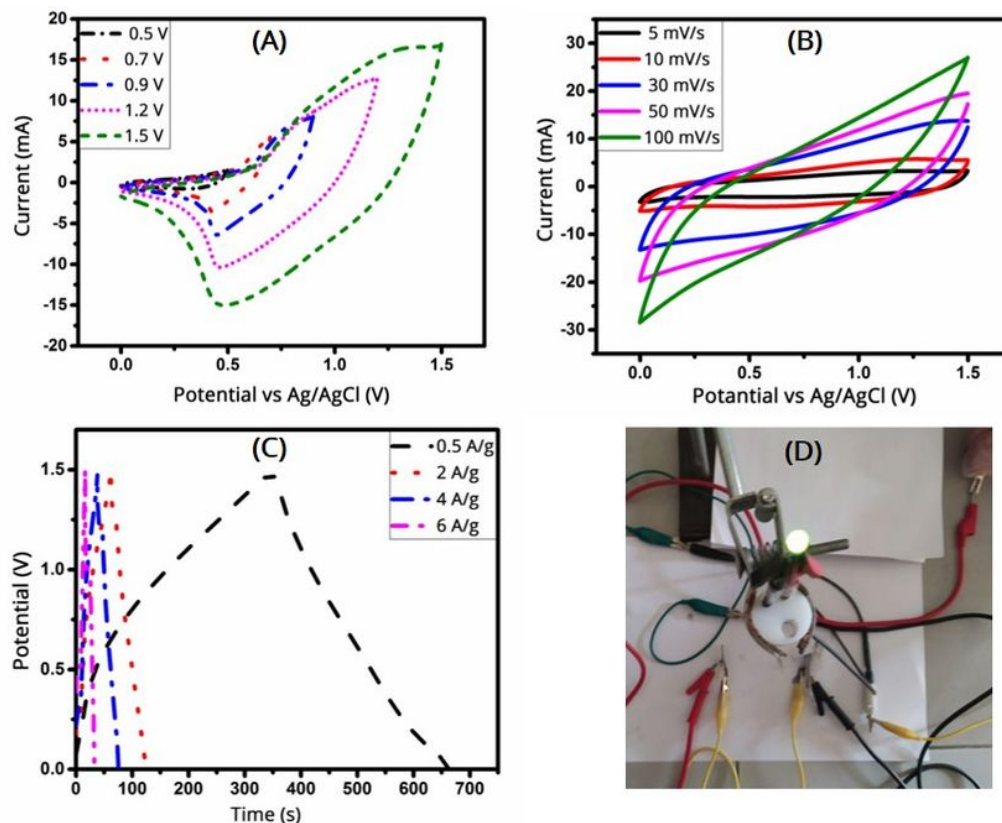


Figure 8

CV curves of the (MnFe₂O₄/MoS₂)//AC asymmetric supercapacitor (A) for different potential windows at 20 mV/s and (B) for different scan rates at the potential window of 1.5 V. (C) GCD curves of the supercapacitor at different current densities at the potential window of 1.5 V. (D) A picture of the assembled asymmetric supercapacitor lighting up a green LED.

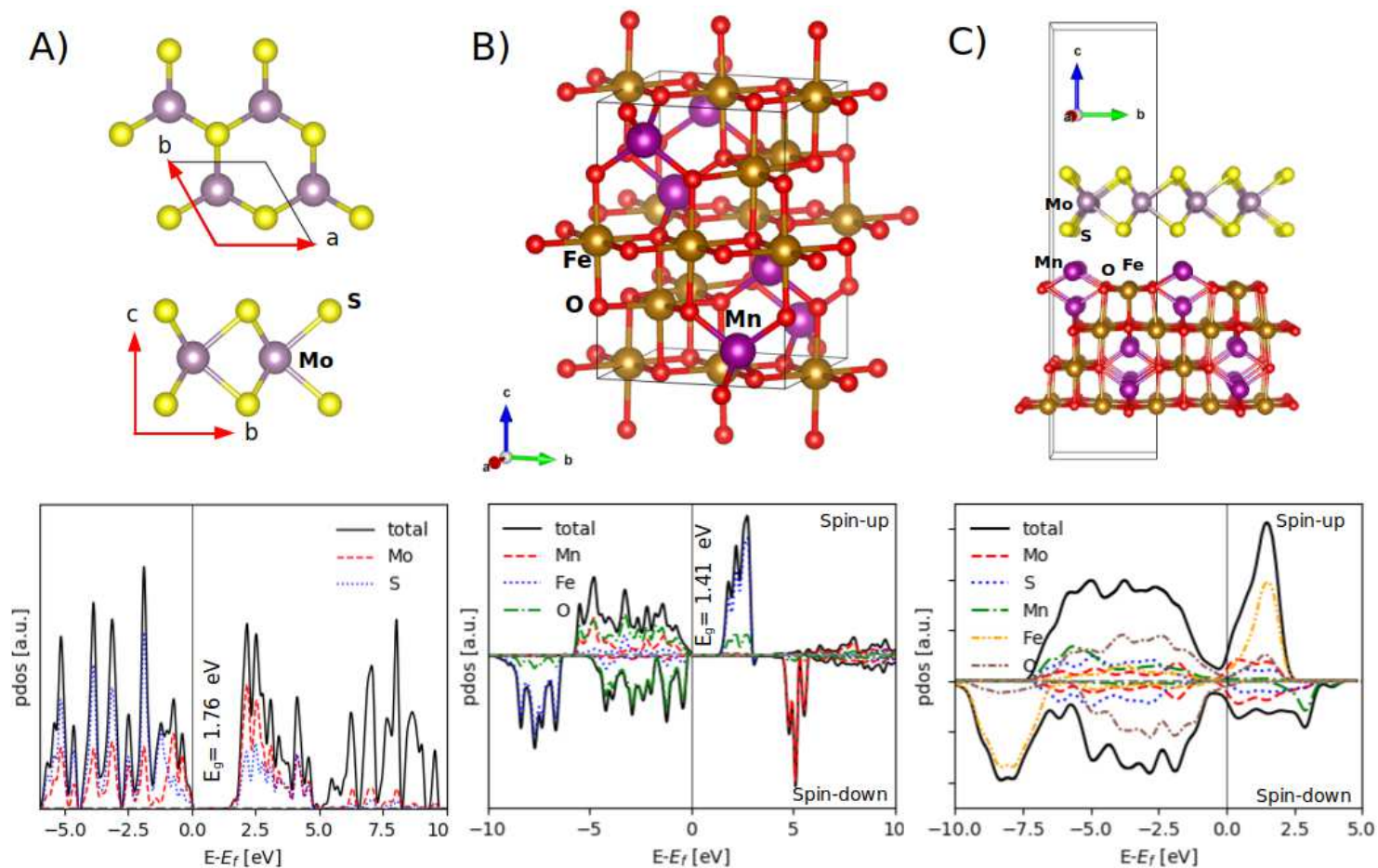


Figure 9

The unit cells and the atom-projected density of states of (A) the MoS₂ monolayer, (B) the normal spinel MnFe₂O₄, and (C) the MnFe₂O₄/MoS₂ interface.

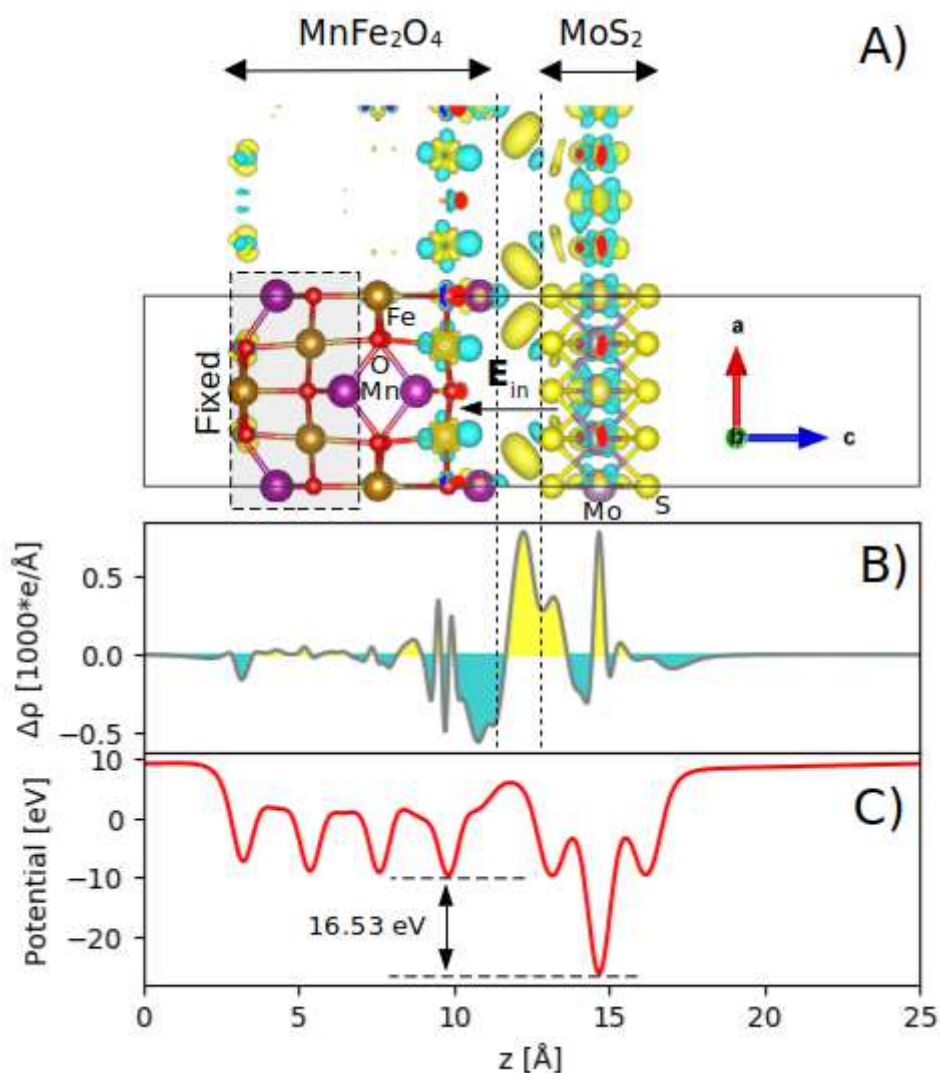


Figure 10

(Color online) (A) A 3D picture of the differential charge density of the MnFe₂O₄/MoS₂ interface, where the yellow and blue areas denote the gain and the loss of electrons, respectively, with the isosurface value of 0.016 e/Å³, with (B) its corresponding in-plane averaged differential charge density along the z -direction. The space between the dashed lines contains no atom. (C) The in-plane averaged electrostatic potential of the MnFe₂O₄/MoS₂ interface.

Supplementary Files

This is a list of supplementary files associated with this preprint. Click to download.

- [Supplementarymaterial.docx](#)
- [graphicalabstract.jpg](#)